Combining PET with MRI to improve predictions of progression from mild cognitive impairment to Alzheimer's disease: an exploratory radiomic analysis study

Fan Yang[1#], Jiehui Jiang[2], Ian Alberts[3#], Min Wang[1#], Taoran Li[4], Xiaoming Sun[1], Axel Rominger[3], Chuantao Zuo[5,6], Kuangyu Shi[3,7]; for the Alzheimer's Disease Neuroimaging Initiative*

[1]Institute of Biomedical Engineering, School of Information and Communication Engineering, Shanghai University, Shanghai, China; [2]Institute of Biomedical Engineering, School of Life Science, Shanghai University, Shanghai, China; [3]Department of Nuclear Medicine, University Hospital Bern, Bern, Switzerland; [4]Department of Neurology, Xuanwu Hospital of Capital Medical University, Beijing, China; [5]PET Center, Huashan Hospital, Fudan University, Shanghai, China; [6]Human Phenome Institute, Fudan University, Shanghai, China; [7]Department of Informatics, Technische Universität München, Munich, Germany

Contributions: (I) Conception and design: F Yang, J Jiang, I Alberts, M Wang; (II) Administrative support: J Jiang, C Zuo; (III) Provision of study materials or patients: C Zuo; (IV) Collection and assembly of data: F Yang, M Wang; (V) Data analysis and interpretation: M Wang, I Alberts, F Yang, A Rominger, K Shi, T Li, X Sun; (VI) Manuscript writing: All authors; (VII) Final approval of manuscript: All authors.

[#]These authors contributed equally to this work.

Correspondence to: Jiehui Jiang. Institute of Biomedical Engineering, School of Life Science, Shanghai University, 98 Shangda Road, Baoshan District, Shanghai 200444, China. Email: jiangjiehui@shu.edu.cn; Chuantao Zuo. PET Center, Huashan Hospital, Fudan University, 12 Middle Urumqi Road, Jing'an District, Shanghai 200040, China. Email: zuochuantao@fudan.edu.cn.

Background: This study aimed to explore the potential of a combination of 18F-fluorodeoxyglucose positron emission tomography (^{18}F-FDG PET) and magnetic resonance imaging (MRI) to improve predictions of conversion from mild cognitive impairment (MCI) to Alzheimer's disease (AD). The predictive performances and specific associated biomarkers of these imaging techniques used alone (single-modality imaging) and in combination (dual-modality imaging) were compared.

Methods: This study enrolled 377 patients with MCI and 94 healthy control participants from 2 medical centers. Enrolment was based on the patients' brain MRI and PET images. Radiomic analysis was performed to evaluate the predictive performance of dual-modality ^{18}F-FDG PET and MRI scans. Regions of interest (ROIs) were determined using an a priori brain atlas. Radiomic features in these ROIs were extracted from the MRI and ^{18}F-FDG PET scan data. These features were either concatenated or used separately to select features and construct Cox regression models for prediction in each modality. Harrell's concordance index (C-index) was then used to assess the predictive accuracies of the resulting models, and correlations between the MRI and ^{18}F-FDG PET features were evaluated.

Results: The C-indices for the two test datasets were 0.77 and 0.80 for dual-modality ^{18}F-FDG PET/MRI, 0.75 and 0.73 for single-modality ^{18}F-FDG PET, and 0.74 and 0.76 for single-modality MRI. In addition, there was a significant correlation between the crucial image signatures of the different modalities.

Conclusions: These results indicate the value of imaging features in monitoring the progress of MCI in populations at high risk of developing AD. However, the incremental benefit of combining ^{18}F-FDG PET and MRI is limited, and radiomic analysis of a single modality may yield acceptable predictive results.

Keywords: Mild cognitive impairment (MCI); magnetic resonance imaging (MRI); positron emission tomography (PET); Cox model; radiology

* Data used in preparation of this article were obtained from the Alzheimer's Disease Neuroimaging Initiative (ADNI) database (adni.loni.usc.edu).

Submitted Aug 18, 2021. Accepted for publication Dec 19, 2021.
doi: 10.21037/atm-21-4349
View this article at: https://dx.doi.org/10.21037/atm-21-4349

Introduction

Alzheimer's disease (AD) is the most common neurodegenerative disease, and mild cognitive impairment (MCI) is a high-risk prodromal stage of AD (1,2). The neuropathological substrates of MCI can be heterogeneous: some patients with MCI may not experience disease progression, some may return to normal, while others may develop AD (3,4). This study aimed to make a significant contribution to the evaluation of risk factors used to predict MCI conversion to AD.

In recent years, neuroimaging modalities have been instrumental in solidifying our understanding of the clinical diagnosis of AD. These modalities include magnetic resonance imaging (MRI) and positron emission tomography (PET), which have attracted the attention of researchers focusing on MCI and AD (5,6). MRI-based structural biomarkers that target gray matter atrophy or shape alterations are those most commonly used in the early biomarker-based detection of AD (7,8) ^{18}F-fluorodeoxyglucose PET (^{18}F-FDG PET) imaging is relatively sensitive and can be used to assess brain glucose metabolism in patients with MCI (7). However, the need for dual-modality or even multimodality techniques to predict MCI conversion to AD has not been conclusively supported. While multimodality imaging can provide a more accurate evaluation of most brain diseases, false-positive results may hinder the implementation of hybrid techniques in the clinical setting, and thus dual-modality imaging for the prediction of MCI conversion to AD is a topic of ongoing research that has yet to be fully evaluated (9,10).

Radiomic analysis aims to extract a large number of quantitative features from medical imaging data and establish statistical models that assist in disease diagnosis, prognosis, and treatment monitoring, thus enhancing the clinical decision-making process (11,12). In recent years, this methodology has been applied in early AD diagnosis and MCI conversion prediction (8,13-17). According to previous research, the accuracy of radiomics-based classification is relatively stable but remains at an exploratory stage. For example, although different modalities provide complementary information for MCI prediction and classification (18,19), the predictive accuracy of a multimodality technique in hybrid imaging has only been partially investigated.

The primary objective of the present study was to explore the potential of dual-modality ^{18}F-FDG PET and MRI scans to predict MCI conversion to AD. We compared the predictive performance of both single-modality imaging techniques with a dual-modality approach. We also investigated the degree to which imaging-derived biomarkers were comparable between these modalities. We present the following article in accordance with the MDAR (Materials Design Analysis Reporting) reporting checklist (available at https://atm.amegroups.com/article/view/10.21037/atm-21-4349/rc).

Methods

The experimental design framework used in this study is outlined in *Figure 1*. First, structural MRI and ^{18}F-FDG PET scans were preprocessed. Eighty cortical regions from the automated anatomical labeling (AAL) atlas were used as regions of interest (ROIs). Radiomics features were extracted and selected using single or dual modalities, and the selected features were then used to construct a Cox proportional hazards model to compare the predictive performance of the different modalities. In addition, a correlation analysis was performed to assess the correlation between the features of the ^{18}F-FDG PET and MRI models.

Participants and image preprocessing

Participants were recruited from 2 independent medical centers. Cohort A comprised 355 patients with MCI and 94 healthy control participants (HCs) whose data were collected from the Alzheimer's Disease Neuroimaging Initiative (ADNI) database (http://adni.loni.usc.edu/). Cohort B comprised 22 patients with MCI whose data were collected from the Department of Neurology at the Huashan Hospital in Shanghai, China. Demographic and clinical information, including education, age, sex, Mini-Mental State Examination (MMSE) scores, time for conversion to AD, and brain scans, were collected for the two cohorts. Patients with MCI were categorized into two groups: an MCI non-converter (MCI-nc) group (n=187), which included participants whose MCI did not convert

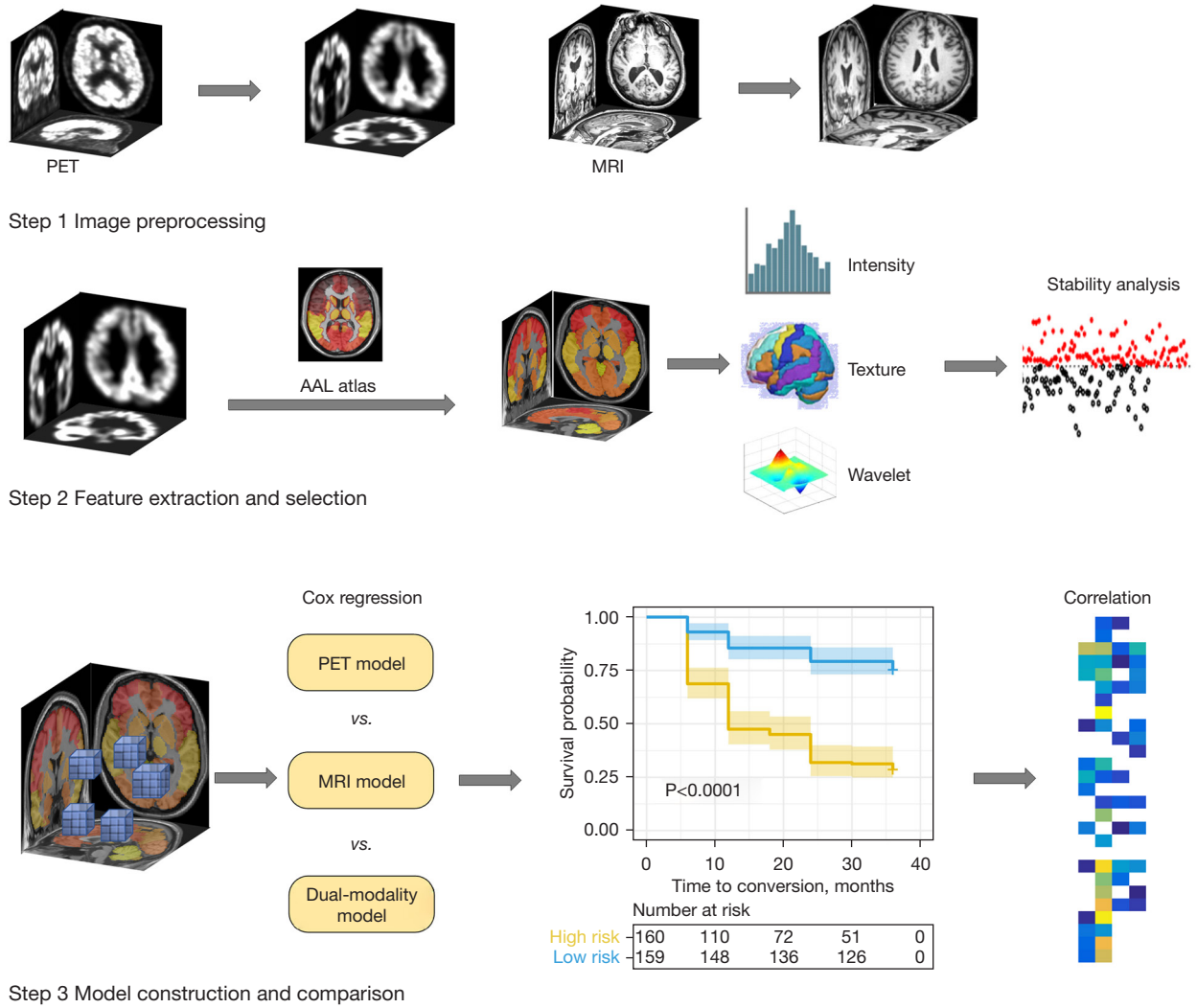

Figure 1 The framework of the experimental design in our study. PET, positron emission tomography; MRI, magnetic resonance imaging; AAL, anatomical automatic labeling.

to AD during the 3-year follow-up, and an MCI converter (MCI-c) group (n=168), which included those whose MCI converted to AD within the 3-year follow-up. Participants who had a biphasic change in diagnosis during follow-up in which MCI converted to AD and returned to MCI were excluded from the analysis. Cohort A contained MRI and ^{18}F-FDG PET scan data from the 94 HCs obtained at 2 points in time with an average interval of 2 years. These data were used to perform a stability analysis of the radiomic features. In total, 355 patients with MCI were also included in cohort A. Cohort B comprised 10 MCI-c and 12 MCI-nc participants. The participants had both MRI and ^{18}F-FDG PET imaging data. During the follow-up period, participants in the MCI-nc group remained clinically stable, while those in the MCI-c group converted to AD during an average follow-up period of 24.5±9.6 months. Data inclusion criteria and acquisition protocol information are detailed further in the Supplementary file (Appendix 1).

Once acquired, all ^{18}F-FDG PET and MRI scans were preprocessed as described previously (17) (Figures S1,S2). This study was approved by the Research Ethics Committee of Huashan Hospital (No. KY2013-336) and was carried out in accordance with the Declaration of Helsinki (as revised in 2013). Informed consent was obtained from all participants in Cohort B or their legal guardians prior to participation.

Image preprocessing was performed using Statistical Parametric Mapping 12 (SPM 12, https://www.fil.ion.ucl.ac.uk/spm/). The original ^{18}F-FDG PET scans were

registered to corresponding structural MRI scans and corrected for the partial volume effect (PVE) with the voxel-wise Muller-Gartner method. The MRI images were segmented using a unified segmentation method. Next, the MRI images, gray matter masks, and ^{18}F-FDG PET images were warped to the Montreal Neurological Institute (MNI) space. Finally, the normalized PET images were smoothed using an isotropic Gaussian kernel of 8 mm.

Radiomic feature extraction and selection

In the feature extraction process, 80 cortical regions from the AAL atlas were defined as the ROIs (20). A radiomics tool developed by Vallières (21) (https://github.com/mvallieres/radiomics) was used, and 430 radiomic features were extracted from each ROI for the MRI and ^{18}F-FDG PET images. Finally, 68,800 features were extracted from the images of each participant. The extracted features included intensity and textural features, as described in the Supplementary file (Appendix 1).

Feature selection was preceded by 10-fold cross-validation, with 90% of the data included as the training dataset and 10% included as the test dataset in each fold, and by the elimination of unit restriction for each feature value through normalization to zero mean and unit standard deviation.

Feature selection was performed using the following steps: (I) feature reliability analysis; (II) statistical testing; and (III) top feature selection. The feature reliability analysis was based on the HCs from cohort A. Cronbach's alpha coefficient was used to evaluate the stability of the features, and stable features with a coefficient greater than 0.75 were selected. Each participant in the HC group had feature sets evaluated at 2 points in time. The most discriminative features between the MCI-c and MCI-nc groups were selected for statistical testing. We used 2-sample *t*-tests and rank-sum tests to identify the features with significant differences between participants in the MCI-c and MCI-nc groups ($P<0.01$). Finally, the top features were selected, and an L1-penalized Cox model was constructed from the training dataset using least absolute shrinkage and selection operator (LASSO) regression. LASSO is a robust method that is especially suitable for the regression of high-dimensional features in a radiomic strategy, and patient features were selected based on the associations with the survival endpoints and time (22). After feature selection, a prediction model was constructed, and 10-fold cross-validation was performed with 200 repetitions in the feature selection stage.

Cox regression model construction

Our prediction model was an L1-penalized Cox regression model. Typical features were selected during the training phase and used to construct the final Cox model. Cox regression is a statistical analysis method that combines clinical outcomes and the time taken by an outcome to appear. In this study, the clinical outcome was conversion from MCI to AD. The time taken by the outcome to appear was the interval between baseline and endpoint. For each participant, the baseline was established as the date of their MRI and PET scans, and the endpoint was either the time of AD diagnosis (for the MCI-c group) or the last follow-up appointment (for the MCI-nc group).

The "glmnet" and "survival" packages (23-25) in R were used to construct the Cox model (http://www.R-project.org/). We used Harrell's concordance index (C-index) to evaluate the model's predictive performance. The C-index was calculated for the training and test datasets. The prognostic index (PI), a linear combination of the selected features and their coefficients, was calculated for each participant in the test dataset using the Cox model and used to calculate the C-index for that dataset. To evaluate the predictive performance of the Cox model in an unbiased manner, 10-fold cross-validation was repeated 20 times, and an average C-index (with the standard deviation values) was calculated. The number of times each feature was repeated in the model construction was counted, and those that repeated in the prediction model for more than two-thirds of the time were selected. These "conserved" features were used for further analyses.

To further compare the predictive performance of these features using single- and dual-modality PET and MRI, we calculated the PI of each participant according to the corresponding modality. Individuals were then stratified into high- and low-risk groups based on the median PI. Survival differences in the risk groups were examined using a log-rank test, and Kaplan-Meier survival curves were also plotted.

Comparison classification

To compare the predictive performances of the different modalities, a single-modality Cox model was constructed using features solely from the MRI or ^{18}F-FDG PET scans, while a dual-modality Cox model was constructed using their combined features. The traditional PET model was constructed by calculating the average FDG standardized uptake value ratio (SUVR), and the MRI model was constructed by calculating the global gray matter volume (GMV). In addition, we used

Table 1 Demographic and clinical characteristics of the study cohorts

Information	MCI					HCs				
	MCI-c (n=168)		MCI-nc (n=187)		P value	Time_1 (n=94)		Time_2 (n=94)		P value
	Median (IQR)	Mean (SD)	Median (IQR)	Mean (SD)		Median (IQR)	Mean (SD)	Median (IQR)	Mean (SD)	
Cohort A: ADNI										
N	168		187			94		94		
Sex (M/F)	95/73		109/78		0.740[a]	48/46		48/46		1[a]
Age (years)	74.4 (9.2)	74.0 (7.1)	72.3 (10.7)	72.1 (7.5)	0.018[b]*	72.5 (8.6)	72.8 (5.9)	74.5 (8.6)	74.8 (5.9)	0.022[b]*
Education (years)	16.0 (4.0)	16.0 (2.6)	16.0 (4.0)	16.0 (2.6)	0.910[b]	17.0 (3.0)	16.9 (2.4)	17.0 (3.0)	16.9 (2.4)	1[b]
MMSE	27.0 (3.0)	26.5 (2.2)	28.0 (2.0)	28.0 (1.6)	<0.001[b]*	30.0 (1.0)	29.2 (1.2)	30.0 (1.0)	29.1 (1.3)	0.766[b]
MoCA	21.0 (3.7)	21.0 (2.8)	21.0 (4.3)	21.1 (2.7)	0.870[b]	26.0 (3.0)	25.9 (2.1)	26.0 (3.0)	25.8 (2.0)	0.873[b]
ADAS-Cog 13	20.3 (7.7)	20.7 (6.5)	20.5 (6.8)	20.9 (6.3)	0.641[b]	9.0 (6.0)	8.6 (3.9)	9.0 (6.0)	8.5 (3.7)	0.732[b]
Conversion time (months)	12.0 (18.0)	14.1 (8.9)	–	–	–					
Cohort B: Huashan Hospital										
N	10		12							
Sex (M/F)	6/4		5/7		0.392[a]					
Age (years)	72.7 (7.6)	73.5 (4.1)	65.0 (10.0)	64.3 (5.7)	<0.001[b]*					
Education (years)	13.5 (4.0)	13.7 (2.3)	12.0 (4.0)	11.9 (2.9)	0.132[b]					
MMSE	26.0 (1.0)	25.5 (2.2)	27.0 (2.0)	26.9 (1.6)	0.100[b]					
MoCA	22.0 (4.0)	21.3 (3.2)	23.0 (3.0)	22.5 (2.4)	0.743[b]					
Conversion time (months)	23.3 (11.9)	24.5 (9.6)	–	–	–					

[a], Chi-square; [b], 2-sample *t*-tests; *, P<0.05. MCI, mild cognitive impairment; ADNI, Alzheimer's Disease Neuroimaging Initiative; MCI-c, MCI converters; MCI-nc, MCI non-converters; HCs, healthy control participants; IQR, interquartile range; SD, standard deviation; MMSE, Mini-Mental State Examination; MoCA, Montreal Cognitive Assessment; ADAS-Cog 13, Alzheimer's Disease Assessment Scale-Cognitive 13.

the participants' demographic information (age, sex, number of years of education) and MMSE scores to construct a clinical Cox model to compare the effects imaging and basic clinical factors may have on the risk of MCI conversion to AD.

Correlation verification of crucial image signatures between different modalities

In this study, conserved features from the ^{18}F-FDG PET and MRI models were considered crucial image signatures, and the relationship between the image signatures of different modalities was further explored. Correlation coefficients between the crucial PET and MRI features were calculated.

Statistical analysis

Descriptive statistics of the continuous variables are expressed as the mean ± standard deviation, and a 2-sample *t*-test was used to compare the differences between the two groups. A chi-squared test was used to illustrate the differences in qualitative variables. Partial correlation coefficients were used to evaluate the correlation between radiomic ^{18}F-FDG PET and MRI features to adjust for age and sex effects. Survival differences in the different risk groups were evaluated using a log-rank test. P values were 2-tailed, and statistical significance was set at P<0.01. MATLAB 2016b (MathWorks Inc., Natick, MA, USA) was used to perform all the statistical tests.

Results

Participants

Table 1 shows the demographic and clinical details of the two cohorts. Significant differences between the MCI-c and

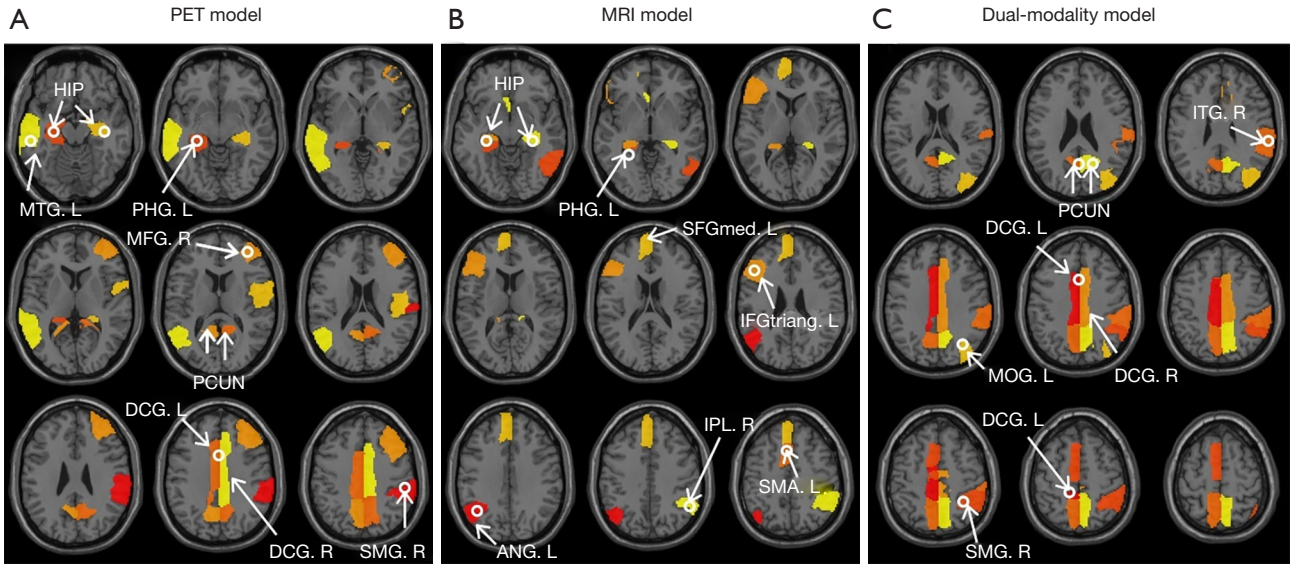

Figure 2 The different brain regions of the features conserved by different radiomic models: (A) the radiomic PET model, (B) the radiomic MRI model, (C) the dual-modality model. PET, positron emission tomography; MRI, magnetic resonance imaging; L, left; R, right; MTG, middle temporal gyrus; HIP, hippocampus; PHG, parahippocampal gyrus; MFG, middle frontal gyrus; PCUN, precuneus; DCG, median cingulate and paracingulate gyrus; SMG, supramarginal gyrus; SFGmed, superior frontal gyrus, medial; IFGtriang, inferior frontal gyrus, triangular part; IPL, inferior parietal; SMA, supplementary motor area; ITG, inferior temporal gyrus; MOG, middle occipital gyrus.

MCI-nc groups in cohort A were observed in age (P=0.018) and MMSE scores (P<0.001), while significant differences were observed only with regard to age in cohort B (P<0.001). There were no significant differences in sex or education levels among the different groups.

Conserved features in different modalities

Features included in the prediction model for more than two-thirds of the time were selected. The numbers of conserved features identified in the single-modality PET and MRI models and the dual-modality model were 13, 12, and 14, respectively. The conserved features of the ^{18}F-FDG PET model were primarily derived from the textural features of the cingulate cortex, hippocampus, parahippocampal gyrus, precuneus, and other temporoparietal regions. For the MRI model, the conserved features were mainly derived from the hippocampus, parahippocampal gyrus, and inferior parietal lobe. Overlapping regions of the conserved features included the bilateral hippocampus and the parahippocampal gyrus, indicating that these regions showed structural changes and metabolic abnormalities.

Most of the conserved features in the dual-modality model overlapped with those in the single-modality models. The conserved features from the MRI images were mainly distributed in the inferior temporoparietal regions. The repeated appearance of these features suggested that they could effectively predict MCI conversion with excellent reproducibility. *Figure 2* shows the distribution of conserved features across the brain regions in the 3 models. All conserved features from the MRI, ^{18}F-FDG PET, and dual-modality models are listed in Table S1, with the crucial image signatures in Table S2. In addition, we have explained the meaning of these conserved features and the direction of changes in the Supplementary file (Appendix 1).

Radiomic analysis predicted MCI conversion to AD

Six prediction models, namely the SUVR_PET model, the GMV_MRI model, the radiomic PET model, the radiomic MRI model, the radiomic dual-modality model, and the clinical model, were constructed. Overall, in cohort A, image-based models (SUVR_PET, GMV_MRI, and the radiomic single- and dual-modality models) were superior to the clinical model, while the radiomic dual-modality model was superior to the radiomic single-modality imaging models. Conversely, the GMV_MRI model and SUVR_

Table 2 Predictive performance of each model

Model	Cohort A training	Cohort A testing	Cohort B
Clinical	0.692 (0.0004)	0.684 (0.006)	0.685 (0.006)
SUVR_PET	0.791 (0.002)	0.751 (0.007)	0.700 (0.004)
GMV_MRI	0.803 (0.003)	0.749 (0.008)	0.702 (0.007)
Radiomic PET	0.871 (0.004)	0.753 (0.008)	0.734 (0.011)
Radiomic MRI	0.807 (0.004)	0.741 (0.007)	0.760 (0.009)
Radiomic dual-modality	0.884 (0.004)	0.766 (0.009)	0.798 (0.008)

C-indices are expressed as the mean (standard deviation) as derived from multiple 10-fold cross-validation in each model. SUVR, standardized uptake value ratio; PET, positron emission tomography; GMV, gray matter volume; MRI, magnetic resonance imaging.

PET model had similar predictive performances. Similar results were also found in cohort B. *Table 2* summarizes the evaluations of predictive performance for each model.

As a result, some of the conserved features from the ^{18}F-FDG PET and MRI models overlapped in the hippocampus and parahippocampal gyrus. To further evaluate the predictive performance of these crucial image signatures, they were used as predictors to construct an independent conventional Cox model for each of the following imaging modalities. Four crucial image signatures distributed in the hippocampus and parahippocampal gyrus on the ^{18}F-FDG PET images were included, as were four crucial image signatures from the MRI images (Table S2). The results indicated that these conserved features could effectively predict the risk of conversion to AD in individuals with MCI.

Survival differences in the low-risk and the high-risk groups were significant in the training and test datasets (log-rank tests, P<0.01). *Figure 3* shows the characteristics of each Cox model and the corresponding Kaplan-Meier survival curves. The Akaike information criterion (AIC) test was used to evaluate the quality of the Cox models (radiomic PET: 1,584.59; radiomic MRI: 1,603.48; dual-modality: 1,572.27). For the validation dataset (cohort B), we evaluated whether the risk groups were better classified according to the PI derived from each model. The 3 models demonstrated good performance in differentiating between the groups with high and low risks of conversion to AD (PET model: P<0.001; MRI model: P=0.007; dual-modality model: P<0.001).

Correlation between different model feature signatures

In this study, we obtained 13 conserved features in the radiomic PET model [Table S1 (a)] and 12 conserved features in the MRI model [Table S1 (b)]. We calculated the correlation coefficients and obtained a 13×12 correlation matrix. Of these paired correlation matrices, 83 showed significant correlations in cohort A (P<0.001; *Figure 4A*), and 4 showed significant correlations in cohort B (P<0.001; *Figure 4B*). Among them, there were 4 pairs of features that were related in all cohorts and modalities, as shown in the red box in *Figure 4*. On the ^{18}F-FDG PET images, these features were in the parahippocampal (busyness), cingulum_mid [zone percentage (ZP)], large zone low gray-level emphasis (LZLGE), and cingulum_mid [large zone emphasis (LZE)]. On the MRI images, they were in the angular gyrus [run percentage (RP)], hippocampus (coarseness), and olfactory cortex (coarseness).

Discussion

This study used radiomic analysis to compare the capabilities of single-modality MRI and ^{18}F-FDG PET and dual-modality MRI to predict the MCI conversion to AD. One strength of this study was that we used two separate cohorts from Western (ADNI) and Chinese (Huashan) populations. Although the sample size of the Huashan dataset was somewhat small as an external test dataset whose inclusion might have therefore led to overfitting and inconsistent results among the different modalities, our findings verified the feature stability across different ethnic cohorts.

We showed that dual-modality imaging is useful but not necessary for the prediction of MCI conversion to AD. We constructed 6 LASSO models based on the sources of the features. Image-based prediction models showed superior performance to the clinical model. Notably, the radiomic PET/MRI models had better predictive performance

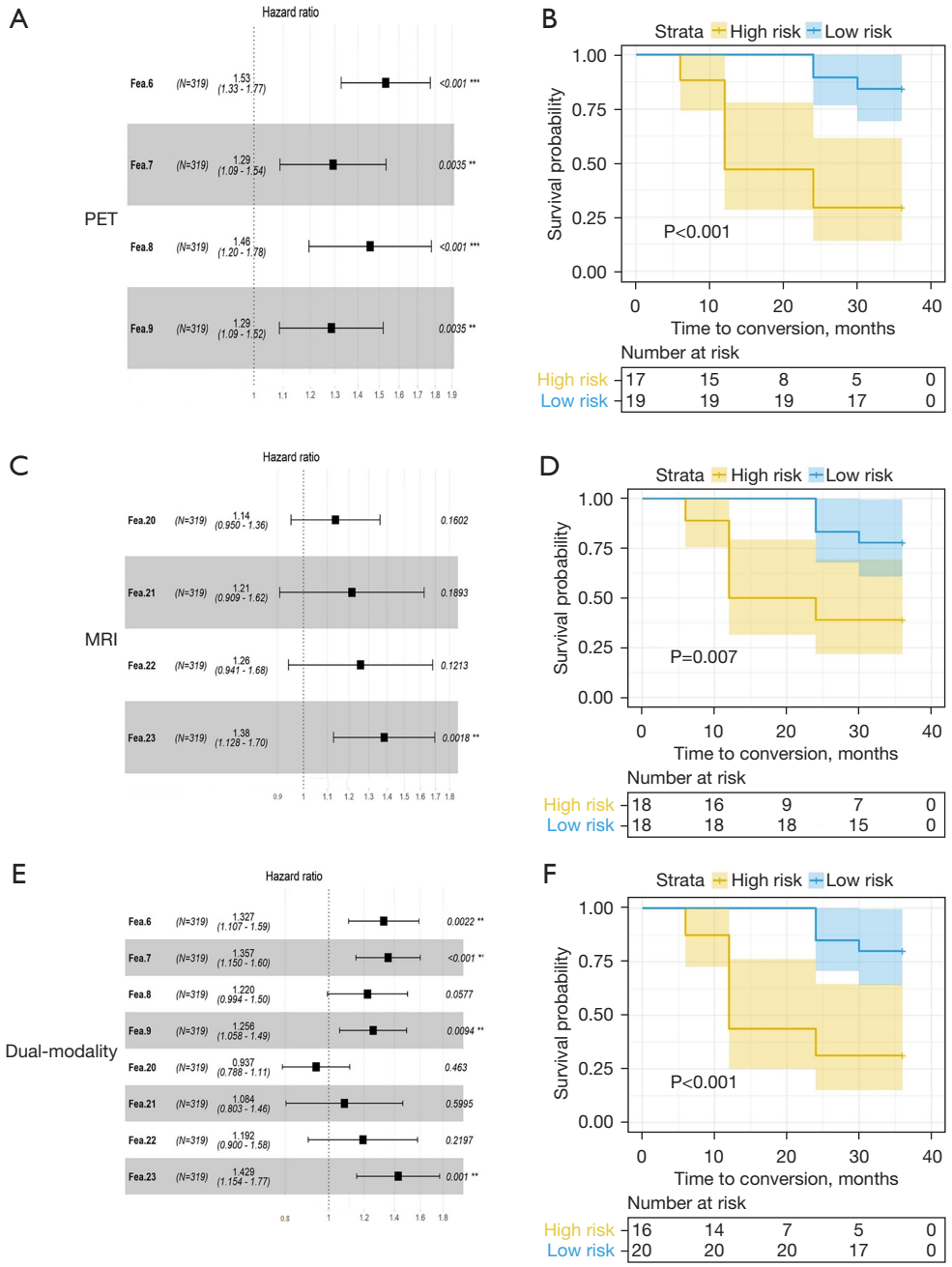

Figure 3 Hazard ratios for different predictors and Kaplan-Meier survival curves for each model. (A) Hazard ratios for different predictors in the PET model with 4 features from the hippocampus and parahippocampal gyrus on PET images as predictors (Fea. 6, Fea. 7, Fea. 8, and Fea. 9, corresponding to features 6, 7, 8, and 9, respectively, in Table S2). Global P value (log-rank), 1.5514e-20; Akaike information criterion (AIC), 1,584.59; C-index, 0.75. (B) Risk stratification of the test dataset in the PET model (log-rank test, P=0.00027). (C) Hazard ratios in the MRI model with 4 features from the hippocampus and parahippocampal gyrus in MRI images as predictors (Fea. 20, Fea. 21, Fea. 22, and Fea. 23, corresponding to features 20, 21, 22, and 23, respectively, in Table S2). Global P value (log-rank), 1.5955e-16; AIC, 1,603.48; C-index, 0.73. (D) Risk stratification of the test dataset in the MRI model (log-rank test, P=0.007). (E) Hazard ratios in the combined model. Global P value (log-rank), 4.4302e-22; AIC, 1,572.27; C-index, 0.77. Predictors were a combination of features from the hippocampus and parahippocampal gyrus on the PET and MRI images. (F) Risk stratification of the test dataset in the combined model (log-rank test, P=0.00073). **, P<0.01; ***, P<0.001. PET, positron emission tomography; MRI, magnetic resonance imaging.

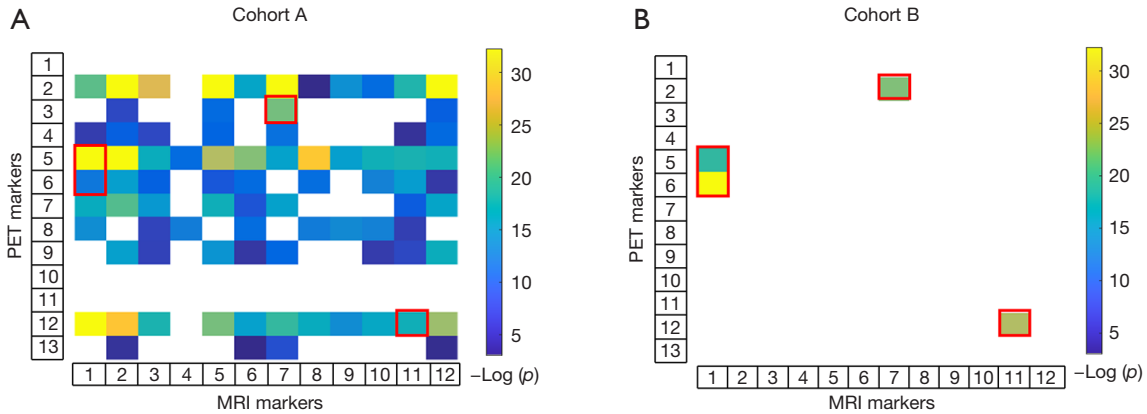

Figure 4 Correlations between 13 conserved features in the PET model and 12 conserved features in the MRI model in cohort A (A) and cohort B (B). The color bar scale represents -log P values. Vertical axis numbers 1–13 represent features in the PET model [consistent with Table S1 (a)], and horizontal axis numbers 1–12 represent features in the MRI model [consistent with Table S1 (b)]. PET, positron emission tomography; MRI, magnetic resonance imaging.

than did the traditional PET/MRI models. This may be due to the lower sensitivity and higher subjectivity of the neuropsychological scales (26). The C-indices of the dual-modality model constructed using data from PET and MRI images were 0.766 for the ADNI participants (cohort A) and 0.798 for the Huashan participants (cohort B) (*Table 2*). These results demonstrate the reliability of the radiomic models for predicting MCI conversion to AD. However, comparison of the single- and dual-modality MRI and PET models revealed that MRI outperformed PET in cohort B (C-indices of 0.760 and 0.734, respectively; P<0.001), while the dual-modality model resulted in only a modest improvement over the single-modality models (C-index of 0.798 for dual-modality *vs.* 0.760 for MRI, and 0.734 for PET; both P<0.001). The cohort A test dataset also showed a modest improvement with the dual-modality model, with PET marginally outperforming MRI in the single-modality models (*Table 2*). The small discrepancies between these results may be attributable to ethnic differences between the Western and Chinese study populations or the uncertainty in the C-index values of cohort B because of the small sample size. Larger studies are required, and no clear recommendation can be made regarding the choice of which single-modality imaging technique to use. Nevertheless, our findings suggest only a modest improvement in predictive capacity can be expected when dual-modality imaging is performed.

Consistent with our hypothesis, most of the conserved features were identified in regions significantly associated with AD, specifically, the medial temporal areas, inferior parietal lobe, precuneus, and cingulate gyrus, which are all brain regions that experience early pathological protein (amyloid-β and hyperphosphorylated tau) deposition (27). They also experience early atrophy, thickness reduction, and metabolic reduction (28-30). Our correlation analyses revealed that some features from different modalities have obvious correlations, indicating the importance of certain regions in the early diagnosis of AD. For example, there was a correlation between the hippocampal features in the 2 modalities, and this region was also correlated with other areas, including the precuneus and the medial cingulate gyrus, which are typical areas of interest in patients with AD.

A recent multicenter study suggested that the hippocampal radiomic features can serve as robust biomarkers for clinical application in predicting MCI conversion to AD (8). The brain regions identified in the present study are in concordance with the regions associated with AD development (13,14,31,32). Several studies have described changes in the hippocampal function as having an impact on the cingulate and precuneus gyrus (33,34). Our study showed a correlation between the textural features of the two regions, indicative of a corresponding pathological correlation. As a result, textural features extracted from these regions were more useful in differentiating between the MCI-c and MCI-nc groups. However, the large degree of overlap identified between the two modalities suggests a large degree of redundancy, with dual-modality imaging providing only a slight gain in information. This fact and the minor improvements in predictive ability indicate that only limited benefits can be expected from dual-modality

PET and MRI imaging. We believe that in resource-poor settings, where patients do not have access to more than 1 imaging modality, or in cases of contraindication or concern about the additional radiation burden encountered in nuclear medicine imaging, single-modality imaging would be acceptable.

This study had some limitations. First, we only used radiomic analysis to verify whether dual-modality imaging is necessary for predicting MCI conversion to AD. Exploration of other methodologies is required to confirm our findings. Second, the radiomic method indicated individual differences between the features. Although the stability of the radiomic features was studied using HCs, the stability of the radiomic features in patients with MCI could be the topic of an ongoing study. Third, the C-index values of cohort B may contain uncertainty in the external test dataset owing to the small sample size. Research must be furthered using external test data with a larger sample size and greater heterogeneity to confirm our findings. Lastly, considering that the ADNI data were used as the training dataset, differences in ethnicity between the training and testing groups should not be ignored.

Conclusions

Comparison of a radiomic model for the prediction of MCI conversion to AD identified a large overlap between ^{18}F-FDG PET and MRI, with much redundancy in dual-modality imaging. The present study showed that the incremental benefit of combining ^{18}F-FDG PET and MRI was limited and that in radiomic models for predicting MCI conversion, single-modality imaging may be sufficient.

Acknowledgments

Funding: This article was supported by grants from the National Natural Science Foundation of China (Nos. 61603236, 81830059, 81971641, 81671239, and 81361120393), the Shanghai Municipal Science and Technology Major Project (Nos. 2017SHZDZX01 and 2018SHZDZX03), and the 111 Project (No. D20031). Data collection and sharing for this project were funded by the Alzheimer's Disease Neuroimaging Initiative (ADNI; National Institutes of Health Grant U01 AG024904) and DODADNI (Department of Defense; No. W81XWH-12-2-0012). ADNI is funded by the National Institute of Aging and the National Institute of Biomedical Imaging and Bioengineering and through generous contributions from the following: AbbVie, Alzheimer's Association; Alzheimer's Drug Discovery Foundation; Araclon Biotech; BioClinica, Inc.; Biogen; Bristol-Myers Squibb Company; CereSpir, Inc.; Eisai, Inc.; Elan Pharmaceuticals, Inc.; Eli Lilly and Company; EuroImmun; F.Hoffmann-La Roche Ltd. and its affiliated company Genentech, Inc.; Fujirebio; GE Healthcare; IXICO Ltd.; Janssen Alzheimer Immunotherapy Research & Development, LLC.; Johnson & Johnson Pharmaceutical Research & Development LLC.; Lumosity; Lundbeck; Merck & Co., Inc.; Meso Scale Diagnostics, LLC.; NeuroRx Research; Neurotrack Technologies; Novartis Pharmaceuticals Corporation; Pfizer, Inc.; Piramal Imaging; Servier; Takeda Pharmaceutical Company; and Transition Therapeutics. The Canadian Institutes of Health Research is providing funds to support ADNI clinical sites in Canada. Private sector contributions are facilitated by the Foundation for the National Institutes of Health (www.fnih.org). The grantee organization is the Northern California Institute for Research and Education, and the study is coordinated by the Alzheimer's Disease Cooperative Study at the University of California, San Diego, CA, USA. ADNI data are disseminated by the Laboratory for Neuro Imaging at the University of Southern California, CA, USA.

Footnote

Reporting Checklist: The authors have completed the MDAR reporting checklist. Available at https://atm.amegroups.com/article/view/10.21037/atm-21-4349/rc

Data Sharing Statement: Available at https://atm.amegroups.com/article/view/10.21037/atm-21-4349/dss

Peer Review File: Available at https://atm.amegroups.com/article/view/10.21037/atm-21-4349/prf

Conflicts of Interest: All authors have completed the ICMJE uniform disclosure form (available at https://atm.amegroups.com/article/view/10.21037/atm-21-4349/coif). The authors have no conflicts of interest to declare.

Ethical Statement: The authors are accountable for all aspects of the work in ensuring that questions related to the accuracy or integrity of any part of the work are appropriately investigated and resolved. This study was approved by the Research Ethics Committee of Huashan Hospital (No. KY2013-336) and was carried out in

accordance with the Declaration of Helsinki (as revised in 2013). Informed consent was obtained from all participants in Cohort B or their legal guardians prior to participation.

References

1. Petersen RC, Doody R, Kurz A, et al. Current concepts in mild cognitive impairment. Arch Neurol 2001;58:1985-92.
2. Li JQ, Tan L, Wang HF, et al. Risk factors for predicting progression from mild cognitive impairment to Alzheimer's disease: a systematic review and meta-analysis of cohort studies. J Neurol Neurosurg Psychiatry 2016;87:476-84.
3. Petersen RC, Roberts RO, Knopman DS, et al. Mild cognitive impairment: ten years later. Arch Neurol 2009;66:1447-55.
4. Schneider JA, Arvanitakis Z, Leurgans SE, et al. The neuropathology of probable Alzheimer disease and mild cognitive impairment. Ann Neurol 2009;66:200-8.
5. Sanchez-Catasus CA, Stormezand GN, van Laar PJ, et al. FDG-PET for Prediction of AD Dementia in Mild Cognitive Impairment. A Review of the State of the Art with Particular Emphasis on the Comparison with Other Neuroimaging Modalities (MRI and Perfusion SPECT). Curr Alzheimer Res 2017;14:127-42.
6. Blazhenets G, Ma Y, Sörensen A, et al. Principal Components Analysis of Brain Metabolism Predicts Development of Alzheimer Dementia. J Nucl Med 2019;60:837-43.
7. Ten Kate M, Ingala S, Schwarz AJ, et al. Secondary prevention of Alzheimer's dementia: neuroimaging contributions. Alzheimers Res Ther 2018;10:112.
8. Zhao K, Ding Y, Han Y, et al. Independent and reproducible hippocampal radiomic biomarkers for multisite Alzheimer's disease: diagnosis, longitudinal progress and biological basis. Science Bulletin 2020;65:1103-13.
9. Suk HI, Shen D, editors. Deep Learning-Based Feature Representation for AD/MCI Classification 2013; Berlin, Heidelberg: Springer Berlin Heidelberg.
10. Hojjati SH, Ebrahimzadeh A, Khazaee A, et al. Predicting conversion from MCI to AD by integrating rs-fMRI and structural MRI. Comput Biol Med 2018;102:30-9.
11. Lambin P, Leijenaar RTH, Deist TM, et al. Radiomics: the bridge between medical imaging and personalized medicine. Nat Rev Clin Oncol 2017;14:749-62.
12. Rizzo S, Botta F, Raimondi S, et al. Radiomics: the facts and the challenges of image analysis. Eur Radiol Exp 2018;2:36.
13. Feng F, Wang P, Zhao K, et al. Radiomic features of hippocampal subregions in Alzheimer's disease and amnestic mild cognitive impairment. Front Aging Neurosci 2018;10:290.
14. Feng Q, Chen Y, Liao Z, et al. Corpus Callosum Radiomics-Based Classification Model in Alzheimer's Disease: A Case-Control Study. Front Neurol 2018;9:618.
15. Feng Q, Song Q, Wang M, et al. Hippocampus Radiomic Biomarkers for the Diagnosis of Amnestic Mild Cognitive Impairment: A Machine Learning Method. Front Aging Neurosci 2019;11:323.
16. Feng Q, Wang M, Song Q, et al. Correlation between hippocampus MRI radiomic features and resting-state intrahippocampal functional connectivity in Alzheimer's disease. Front Neurosci 2019;13:435.
17. Li Y, Jiang J, Lu J, et al. Radiomics: a novel feature extraction method for brain neuron degeneration disease using 18F-FDG PET imaging and its implementation for Alzheimer's disease and mild cognitive impairment. Ther Adv Neurol Disord 2019;12:1756286419838682.
18. Wang P, Chen K, Yao L, et al. Multimodal Classification of Mild Cognitive Impairment Based on Partial Least Squares. J Alzheimers Dis 2016;54:359-71.
19. Liu K, Chen K, Yao L, et al. Prediction of Mild Cognitive Impairment Conversion Using a Combination of Independent Component Analysis and the Cox Model. Front Hum Neurosci 2017;11:33.
20. Seitzman BA, Gratton C, Marek S, et al. A set of functionally-defined brain regions with improved representation of the subcortex and cerebellum. Neuroimage 2020;206:116290.
21. Vallières M, Freeman CR, Skamene SR, et al. A radiomics model from joint FDG-PET and MRI texture features for the prediction of lung metastases in soft-tissue sarcomas of the extremities. Phys Med Biol 2015;60:5471-96.
22. Gui J, Li H. Penalized Cox regression analysis in the high-

dimensional and low-sample size settings, with applications to microarray gene expression data. Bioinformatics 2005;21:3001-8.
23. Simon N, Friedman J, Hastie T, et al. Regularization Paths for Cox's Proportional Hazards Model via Coordinate Descent. J Stat Softw 2011;39:1-13.
24. Friedman J, Hastie T, Tibshirani R. Regularization Paths for Generalized Linear Models via Coordinate Descent. J Stat Softw 2010;33:1-22.
25. Therneau TM, Grambsch PM. Modeling Survival Data: Extending the Cox Model. Modeling Survival Data: Extending the Cox Model, 2013.
26. Huang K, Lin Y, Yang L, et al. A multipredictor model to predict the conversion of mild cognitive impairment to Alzheimer's disease by using a predictive nomogram. Neuropsychopharmacology 2020;45:358-66.
27. Long JM, Holtzman DM. Alzheimer Disease: An Update on Pathobiology and Treatment Strategies. Cell 2019;179:312-39.
28. Kato T, Inui Y, Nakamura A, et al. Brain fluorodeoxyglucose (FDG) PET in dementia. Ageing Res Rev 2016;30:73-84.
29. Pini L, Pievani M, Bocchetta M, et al. Brain atrophy in Alzheimer's Disease and aging. Ageing Res Rev 2016;30:25-48.
30. Risacher SL, Saykin AJ. Neuroimaging in aging and neurologic diseases. Handb Clin Neurol 2019;167:191-227.
31. Bailly M, Destrieux C, Hommet C, et al. Precuneus and Cingulate Cortex Atrophy and Hypometabolism in Patients with Alzheimer's Disease and Mild Cognitive Impairment: MRI and (18)F-FDG PET Quantitative Analysis Using FreeSurfer. Biomed Res Int 2015;2015:583931.
32. Zhou H, Jiang J, Lu J, et al. Dual-Model Radiomic Biomarkers Predict Development of Mild Cognitive Impairment Progression to Alzheimer's Disease. Front Neurosci 2019;12:1045.
33. Papma JM, Smits M, de Groot M, et al. The effect of hippocampal function, volume and connectivity on posterior cingulate cortex functioning during episodic memory fMRI in mild cognitive impairment. Eur Radiol 2017;27:3716-24.
34. Xue J, Guo H, Gao Y, et al. Altered directed functional connectivity of the hippocampus in mild cognitive impairment and Alzheimer's disease: a resting-state fMRI study. Front Aging Neurosci 2019;11:326.

(English Language Editors: L. Roberts and J. Gray)

Cite this article as: Yang F, Jiang J, Alberts I, Wang M, Li T, Sun X, Rominger A, Zuo C, Shi K; for the Alzheimer's Disease Neuroimaging Initiative. Combining PET with MRI to improve predictions of progression from mild cognitive impairment to Alzheimer's disease: an exploratory radiomic analysis study. Ann Transl Med 2022;10(9):513. doi: 10.21037/atm-21-4349

Supplementary

Participants

The inclusion criteria for participants with mild cognitive impairment (MCI) were as follows: (I) participants diagnosed with MCI at the time of data collection; (II) magnetic resonance imaging (MRI) and ^{18}F-fluorodeoxyglucose positron emission tomography (^{18}F-FDG PET) scans collected for each participant. Participants' data were retrieved from the Alzheimer's Disease Neuroimaging Initiative (ADNI) database (cohort A) and the Department of Neurology at Huashan Hospital in Shanghai, China (cohort B), and participants in both cohorts were categorized into 2 groups: an MCI nonconverter (MCI-nc) group, whose MCI did not convert to Alzheimer's disease (AD), and an MCI-converter (MCI-c) group, whose MCI did convert to AD. Cohort A consisted of 168 MCI-cs and 187 MCI-ncs, while cohort B comprised 10 MCI-cs and 12 MCI-ncs. Cohort A also contained the MRI and ^{18}F-FDG PET data of 94 healthy control participants obtained at 2 points in time with an average interval of 2 years. The inclusion criteria for the healthy control participants were as follows: (I) a Mini-Mental State Examination (MMSE) score of between 24 and 30; (II) a clinical dementia rating (CDR) of 0; (III) and no diagnosis of depressions, MCI, or dementia. This data set was used to perform a stability analysis on the radiomic features.

Cohort B comprised 10 MCI-cs and 12 MCI-ncs. Participants in this cohort had both MRI and ^{18}F-FDG PET imaging data. MCI-ncs remained clinically stable, while MCI-cs converted to Alzheimer's disease (AD) during the average follow-up period of 24.5±9.6 months. MCI was diagnosed according to previously published criteria (1).

Acquisition protocol

ADNI (cohort A)

Detailed information on the structural MRI and ^{18}F-FDG PET data acquisition for cohort A can be obtained by visiting the image protocol column of the ADNI dataset on the official website of the ADNI (http://adni.loni.usc.edu/). For the participants in the present study, ^{18}F-FDG PET images were acquired in a resting state 30-35 minutes after the injection of 185±18.5 MBq FDG.

Huashan Hospital (cohort B)

Structural MRI

MRI data for all participants in cohort B were obtained using a 3T MR750 scanner (General Electric Company, Boston, MA, USA). An inversion recovery prepared fast spoiled gradient recalled sequence was used to obtain T1 weighted, high-resolution, 3-dimensional (3D) anatomical brain images. The scanning range was from the cranial crest to the occipital foramen. The scan parameters were as follows: repetition time (TR) =11.1 ms, echo time (TE) =5.0 ms, flip angle =20°, matrix size =256×256, voxel size = 1×1×1 mm^3, field of view (FOV) =240 mm^2, slice thickness = 1.0 mm; 146 slices without slice gap, and transverse acquisition.

https://dx.doi.org/10.21037/atm-21-4349

^{18}F-FDG PET

A Siemens Biograph 64 HD PET/CT scanner was used to perform ^{18}F-FDG PET scanning in 3D mode at resting state (1.5 min/bed, 5 bed positions). All participants were required to have been fasting for at least 6 hours before the examination. Each participant received an intravenous injection of 185 MBq ±37 FDG and rested in a quiet and dark environment for 45 minutes prior to the scan. Before PET scanning, we used low-dose CT transmission scanning to reduce the effects of attenuation.

Data preprocessing protocol

Data preprocessing for the PET and MRI images was performed using the Statistical Parametric Mapping 12 package (SPM12, the Wellcome Department of Neurology, London U.K.) in MATLAB 2016b (MathWorks Inc., Natick, MA, USA).

First, dcm2nii software (http://www.nitrc.org/projects/dcm2nii/) was used to convert digital imaging and communications in medicine (DICOM) files to neuroimaging informatics technology initiative (NIFTI) files. Second, each original 18F-FDG PET scan was registered to a corresponding original structural MRI scan and corrected for partial volume effect (PVE) using the voxel-wise PVE method. Then, the MRI images were segmented using the unified segmentation method. Next, the forward parameters were estimated during the unified segmentation, and the original MRI scan, gray matter (GM) binary mask, and registered PET image were registered to the Montreal Neurological Institute (MNI) stereotaxic template. Finally, the normalized PET scans were smoothed.

^{18}F-FDG PET: each original structural MRI scan was used to register a corresponding original ^{18}F-FDG PET scan. PVE algorithms were used to correct PVE in the PET scans, using the PETPVE12 toolbox, after a voxel-wise method defined by Muller-Gartner *et al.* (2). Our study-specific settings included the specification of an isotropic PSF of 6 mm. The same transformation parameters were used to normalize the registered PET scan to the MNI template. Finally, an isotropic gaussian kernel of 8 mm was used to smooth the normalized PET scans to increase signal-to-noise ratios. Some of the processing results are shown as examples in *Figure S1*.

MRI: the unified segmentation method was used to segment MRI images into gray matter (GM), white matter (WM), and cerebrospinal fluid (CSF) tissue probability maps. Then, the original MRI scan and GM binary mask were registered to the MNI stereotaxic template using the forward parameters. Some processing results are shown as examples in *Figure S1*.

Individual GM binary masks were derived from 50% GM suprathreshold voxels plus those whose GM probability exceeded that of WM and CSF. The final positioning of the brain regions is shown in *Figure S2*. Individual GM binary masks were used to mask the corresponding normalized MRI, and the smoothed 18F-FDG PET scans in the MNI space.

Feature extraction

Texture features [9 from the gray-level co-occurrence matrix (GLCM), 13 from the gray-level run-length matrix (GLRLM), 13 from the gray-level size zone matrix (GLSZM), and 5 from the neighborhood gray-tone difference matrix (NGTDM)] were used to measure tissue heterogeneity by quantitatively describing the spatial distribution of intensities within the regions of interest (ROIs). The first-order intensity features, including variance, skewness, and kurtosis, were calculated according to the intensity distribution of each ROI. All texture features were calculated using 3D analysis (26 neighborhoods). For each texture matrix, only 1 comprehensive texture matrix was calculated by simultaneously considering the adjacent attributes of voxels in 13 directions of 3D space. At the same time, considering discretization length differences, the 6 voxels at a distance of 1 voxel, the 12 voxels at a distance of $\sqrt{2}$ voxels, and the 8 voxels at a distance of $\sqrt{3}$ voxels around the center voxels were treated differently in the calculation of the matrices (3).

The calculation of the texture matrices was dependent on the gray level quantization values since they quantify the relationship between the levels of gray. A reasonable gray level quantization value shortened the calculation time of the feature matrix and improve the signal-to-noise ratio of the texture outcome. Following previous texture analysis research, we selected the number of gray levels (i.e., the dynamic range) as 32 and 64. Wavelet band-pass filtering highlighted detailed information in images at different spatial frequencies. When performing wavelet band-pass filtering, we first performed

https://dx.doi.org/10.21037/atm-21-4349

wavelet decomposition in ROIs on the images in 8 directions (LLL, LLH, LHL, LHH, HLL, HLH, HHL, and HHH), and then defined a coefficient R, indicating the ratio of the weight applied to band-pass sub-bands (LLH, HLH, LHL, HLL, HHL, and LHH) compared to the weight applied to low-frequency and high-frequency sub-bands (LLL and HHH). By adjusting R, and then performing the inverse wavelet transformation, a transformed ROI image was obtained, emphasizing detailed information at different spatial frequencies. Following previous research (4), we extracted wavelet features at 5 spatial frequencies, with R values of 1/2, 2/3, 1 (without wavelet filtering), 3/2, and 2. After selecting the gray level quantization range and wavelet band-pass filter weight (R), we extracted the same number of first-order intensity features and texture features for the processed image.

Finally, we extracted 430 radiomic features from each ROI for each participant's MRI and 18F-FDG PET data. For participants with both MRI and PET scans, a total of 68,800 features were extracted (430×80×2 =68,800). The most basic features in each ROI included first-order intensity features (n=3) and textural features (n=40). By selecting different feature extraction parameters, more features were obtained. We combined different wavelet filter weights (5 levels) and quantization of gray levels (to 2 levels) to extract the features, with 430 features [(3+40)×5×2 = 430] extracted for each ROI.

Conserved features in different modalities

After removing duplicate features, 16 different conserved features remained. The meanings of these features are as follows: the variance feature extracted from the GLCM category is an indicator of dispersion of the unit values around the mean (5); the coarseness feature extracted from the NGTDM has been likened to granularity within an image—that is, coarseness is higher in images of larger granularity and lower in those with a smaller granularity (6); the contrast and busyness features are both derived from the NGTDM and define local texture features by describing the differences between each voxel and the neighboring voxels. Contrast relates to the difference between neighboring regions of voxel intensities, and high contrast in an image indicates that there is a significant difference in voxel intensity between adjacent voxels. Busyness correlates with the change rate between neighborhood intensities weighted by the difference in intensities, and the characteristic of a busy texture is that the intensity of adjacent voxels changes rapidly (7).

https://dx.doi.org/10.21037/atm-21-4349

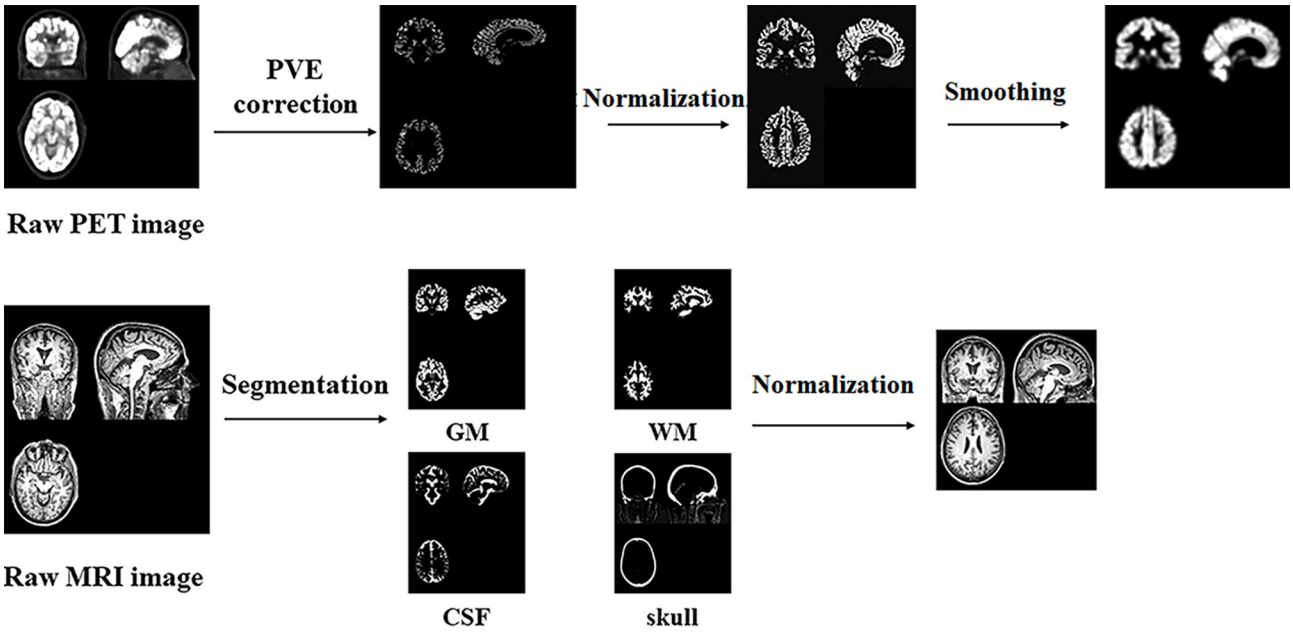

Figure S1 An example of the PET and MRI preprocessing results. PET, positron emission tomography; MRI, magnetic resonance imaging; GM, gray matter; WM, white matter; CSF, cerebrospinal fluid.

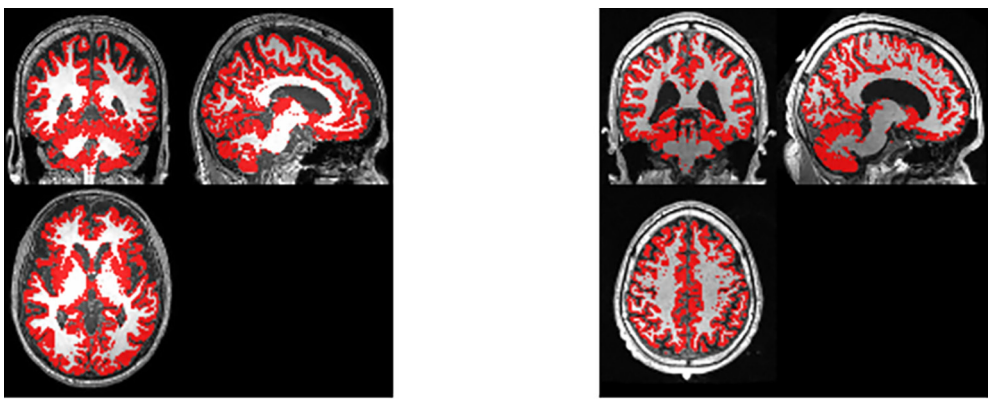

$$((P_{GM} > P_{WM}) \cap (P_{GM} > P_{CSF})) \cup (P_{GM} > 0.5)$$

Figure S2 Final positioning of brain regions. GM, gray matter; WM, white matter; CSF, cerebrospinal fluid.

https://dx.doi.org/10.21037/atm-21-4349

Table S1 Conserved features in the different Cox models

Top	Times	Modality	Labeled number	Labeled region	R	Gray level	Feature name
(a) Single-modality PET model							
1	196	PET	64	SupraMarginal_R	2.00	32	SZHGE
2	194	PET	37	Hippocampus_L	1.50	32	GLV
3	194	PET	39	ParaHippocampal_L	1.00	64	Busyness
4	185	PET	68	Precuneus_R	1.50	64	Correlation
5	181	PET	33	Cingulum_Mid_L	1.50	32	ZP
6	179	PET	33	Cingulum_Mid_L	1.50	32	LZLGE
7	176	PET	67	Precuneus_L	2.00	32	ZSV
8	157	PET	8	Frontal_Mid_R	0.50	32	Skewness
9	144	PET	18	Rolandic_Oper_R	2.00	64	Contrast
10	144	PET	38	Hippocampus_R	1.00	64	Correlation
11	144	PET	68	Precuneus_R	2.00	64	Variance
12	139	PET	34	Cingulum_Mid_R	0.50	64	LZE
13	137	PET	85	Temporal_Mid_L	0.67	64	Contrast
(b) Single-modality MRI model							
1	200	MRI	65	Angular_L	0.50	32	RP
2	198	MRI	39	ParaHippocampal_L	2.00	32	Coarseness
3	196	MRI	90	Temporal_Inf_R	2.00	32	Skewness
4	195	MRI	19	Supp_Motor_Area_L	1.00	64	Strength
5	192	MRI	38	Hippocampus_R	0.50	32	ZP
6	165	MRI	13	Frontal_Inf_Tri_L	0.50	64	Skewness
7	163	MRI	37	Hippocampus_L	1.00	64	Coarseness
8	160	MRI	62	Parietal_Inf_R	1.50	32	Busyness
9	156	MRI	23	Frontal_Sup_Medial_L	0.50	64	Contrast
10	153	MRI	62	Parietal_Inf_R	1.00	64	Skewness
11	147	MRI	21	Olfactory_L	1.50	32	Coarseness
12	134	MRI	38	Hippocampus_R	2.00	32	RLN
(c) Dual-modality model							
1	197	PET	33	Cingulum_Mid_L	1.50	32	ZP
2	191	PET	68	Precuneus_R	1.50	64	Correlation
3	190	MRI	19	Supp_Motor_Area_L	1.00	64	Strength
4	190	MRI	62	Parietal_Inf_R	1.00	64	Skewness
5	188	PET	64	SupraMarginal_R	2.00	32	SZHGE
6	180	PET	67	Precuneus_L	2.00	32	ZSV
7	179	PET	37	Hippocampus_L	1.50	32	GLV
8	174	PET	39	ParaHippocampal_L	1.00	64	Busyness
9	162	PET	34	Cingulum_Mid_R	0.50	64	LZE
10	155	MRI	90	Temporal_Inf_R	2.00	32	Skewness
11	154	PET	52	Occipital_Mid_R	0.50	64	GLN
12	146	PET	39	ParaHippocampal_L	1.00	32	RP
13	146	PET	68	Precuneus_R	2.00	64	Variance
14	138	PET	38	Hippocampus_R	1.00	64	Correlation

Times: the number of times each feature repeated in the 10-fold cross-validation with 200 repetitions of the model construction, R: weights to band-pass subbands in wavelet filtering, gray level: gray level quantization value. SZHGE, small zone high gray-level emphasis; GLV, gray-level variance; ZP, zone percentage; LZLGE, large zone low gray-level emphasis; ZSV, zone-size variance; LZE, large zone emphasis; RP, run percentage; RLN, run-length nonuniformity; GLN, gray-level nonuniformity.

https://dx.doi.org/10.21037/atm-21-4349

Table S2 Crucial image signatures from three image-based models

Top	Modality	Labeled number	Labeled region	R	Gray level	Feature name
1	PET	8	Frontal_Mid_R	0.50	32	Skewness
2	PET	18	Rolandic_Oper_R	2.00	64	Contrast
3	PET	33	Cingulum_Mid_L	1.50	32	ZP
4	PET	33	Cingulum_Mid_L	1.50	32	LZLGE
5	PET	34	Cingulum_Mid_R	0.50	64	LZE
6	PET	37	Hippocampus_L	1.50	32	GLV
7	PET	38	Hippocampus_R	1.00	64	Correlation
8	PET	39	ParaHippocampal_L	1.00	32	RP
9	PET	39	ParaHippocampal_L	1.00	64	Busyness
10	PET	52	Occipital_Mid_R	0.50	64	GLN
11	PET	64	SupraMarginal_R	2.00	32	SZHGE
12	PET	67	Precuneus_L	2.00	32	ZSV
13	PET	68	Precuneus_R	1.50	64	Correlation
14	PET	68	Precuneus_R	2.00	64	Variance
15	PET	85	Temporal_Mid_L	0.67	64	Contrast
16	MRI	13	Frontal_Inf_Tri_L	0.50	64	Skewness
17	MRI	19	Supp_Motor_Area_L	1.00	64	Strength
18	MRI	21	Olfactory_L	1.50	32	Coarseness
19	MRI	23	Frontal_Sup_Medial_L	0.50	64	Contrast
20	MRI	37	Hippocampus_L	1.00	64	Coarseness
21	MRI	38	Hippocampus_R	0.50	32	ZP
22	MRI	38	Hippocampus_R	2.00	32	RLN
23	MRI	39	ParaHippocampal_L	2.00	32	Coarseness
24	MRI	62	Parietal_Inf_R	1.00	64	Skewness
25	MRI	62	Parietal_Inf_R	1.50	32	Busyness
26	MRI	65	Angular_L	0.50	32	RP
27	MRI	90	Temporal_Inf_R	2.00	32	Skewness

Times: the number of times each feature repeated in the 10-fold cross-validation with 200 repetitions of the model construction, R: weights to band-pass subbands in wavelet filtering, gray level: gray level quantization value. ZP, zone percentage; LZLGE, large zone low gray-level emphasis; LZE, large-zone emphasis; GLV, gray-level variance; RP, run percentage; GLN, gray-level nonuniformity; SZHGE, small zone high gray-level emphasis; ZSV, zone-size variance; RLN, run-length nonuniformity.

https://dx.doi.org/10.21037/atm-21-4349

References

1. Dubois B, Feldman HH, Jacova C, et al. Advancing research diagnostic criteria for Alzheimer's disease: the IWG-2 criteria. Lancet Neurol 2014;13:614-29.
2. Müller-Gärtner HW, Links JM, Prince JL, et al. Measurement of radiotracer concentration in brain gray matter using positron emission tomography: MRI-based correction for partial volume effects. J Cereb Blood Flow Metab 1992;12:571-83.
3. Vallières M, Freeman CR, Skamene SR, et al. A radiomics model from joint FDG-PET and MRI texture features for the prediction of lung metastases in soft-tissue sarcomas of the extremities. Phys Med Biol 2015;60:5471-96.
4. Li Y, Jiang J, Lu J, et al. Radiomics: a novel feature extraction method for brain neuron degeneration disease using 18F-FDG PET imaging and its implementation for Alzheimer's disease and mild cognitive impairment. Ther Adv Neurol Disord 2019;12:1756286419838682.
5. Pantic I, Jeremic R, Dacic S, et al. Gray-Level Co-Occurrence Matrix Analysis of Granule Neurons of the Hippocampal Dentate Gyrus Following Cortical Injury. Microsc Microanal 2020;26:166-72.
6. Cheng NM, Fang YH, Chang JT, et al. Textural features of pretreatment 18F-FDG PET/CT images: prognostic significance in patients with advanced T-stage oropharyngeal squamous cell carcinoma. J Nucl Med 2013;54:1703-9.
7. Ahn HK, Lee H, Kim SG, et al. Pre-treatment 18F-FDG PET-based radiomics predict survival in resected non-small cell lung cancer. Clin Radiol 2019;74:467-73.

https://dx.doi.org/10.21037/atm-21-4349